Discovery of Ni activated sintering of MoNbTaW predicted by a computed grain boundary diagram

Sashank Shivakumar [a], Keqi Song [a], Chunyang Wang [b], Tianjiao Lei [c], Huolin L. Xin [b], Timothy J. Rupert [c], Jian Luo [a,*]

[a] Department of NanoEngineering, Program of Materials Science and Engineering, University of California San Diego, La Jolla, CA, 92093, United States of America
[b] Department of Physics and Astronomy, University of California, Irvine, CA 92697, United States of America
[c] Department of Materials Science and Engineering, Department of Mechanical and Aerospace Engineering, University of California, Irvine, CA, 92697, United States of America

ARTICLE INFO

ABSTRACT

Activated sintering of refractory metals represents a classical phenomenon in powder metallurgy. This study discovers that Ni addition can enhance sintering of MoNbTaW both above and below the bulk solidus composition at 1800 °C, thereby demonstrating the first example of activated sintering of a high-entropy alloy. To probe the underlying mechanism, experiments reveal complete grain boundary (GB) wetting above the bulk solidus composition, which logically infers the stabilization of a liquid-like interfacial phase (GB complexion) in a prewetting region below the bulk solidus composition. Furthermore, bulk CALPHAD (calculation of phase diagram) methods have been extended to model GBs in Ni-doped MoNbTaW to compute a GB "phase" diagram to forecast high-temperature GB disordering in the prewetting region and rationalize the observed Ni-activated sintering of MoNbTaW. Only weak GB segregation of Ni is found in furnace-cooled specimens, which suggests GB "drying" during cooling, consistent with the observed nanoscale precipitates along GBs.

Refractory high-entropy or complex concentrated alloys (RHEAs/RCCAs) based on body-centered cubic (BCC) refractory elements such as Mo, Nb, Ta, and W show promising high-temperature mechanical properties that can outperform Ni-based superalloys [1–5]. However, fabrication of RHEAs/RCCAs via either solidification or powder metallurgy routes is generally challenging due to their high melting temperatures. Specifically, sintering dense parts of refractory alloys often requires high temperatures, high pressures, and/or prolonged sintering durations. A common route to enhance sintering of refractory alloys is via liquid phase sintering, which facilitates densification through increased mass transport, capillary action, and particle re-arrangement promoted by the presence of a secondary liquid phase [6]. Notably, it has long been known that addition of small amounts of transition metal "activators" such as Ni can also enhance densification of W, Mo, and Ta well below the bulk solidus curves, a phenomenon termed as solid-state (subsolidus) "activated sintering" [7–11]. Subeutectic activated sintering was also observed in ceramics and attributed to enhanced mass transfer in intergranular films formed by premelting like transitions, first in ZnO-Bi$_2$O$_3$ [12] and subsequently in TiO$_2$—CuO [13]. Premelting and

prewetting 2-D interfacial phases (also termed as "complexions" [14–16]) of similar character have been observed in W-Ni [17] and Mo-Ni [18], which offered an explanation for activated sintering in these refractory metals [19,20]. Interested readers are referred to a critical review [21] that compared impurity-based quasi-liquid interfacial phases in ceramics and metals and discussed related premelting and prewetting phenomena. Furthermore, bulk calculation of phase diagram (CALPHAD) methods have been extended to grain boundaries (GBs) to compute "GB λ diagrams" to forecast high-temperature GB disordering (in premelting and prewetting regions) and related sintering trends [20, 22-27]. Although a more recent study suggested that adding Ni can enhance the densification of refractory high-entropy nanoalloys via spark plasma sintering [28], it is not yet known whether (conventional pressure-less) activated sintering, as well as the underlying interfacial phenomena and predictive tools (computed GB λ diagrams), can be extended to RHEAs/RCCAs, providing motivation for this study.

In this work, we demonstrated Ni activated sintering of MoNbTaW as the first example of pressure-less subsolidus activated sintering of a high-entropy alloy. Subsequently, we computed a GB λ diagram for
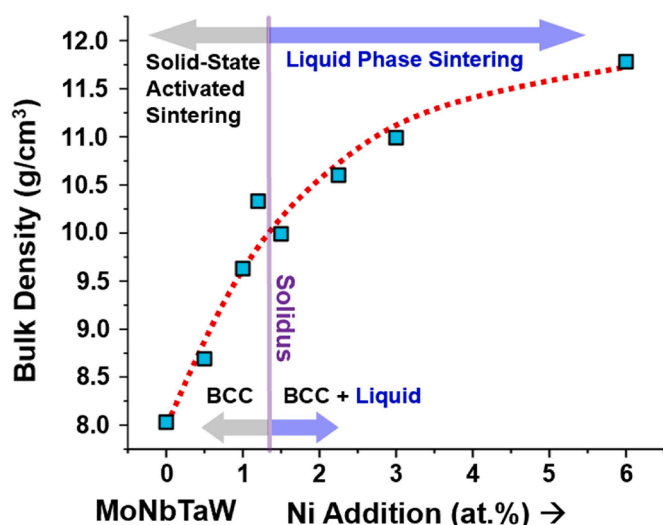
Fig. 1. Measured sintered density *versus* the atomic percent of Ni addition for MoNbTaW based specimens sintered isothermally at 1800 °C for 2 h, showing both subsolidus activated sintering and liquid-phase sintering.

MoNbTaW-Ni (again, for the first time for a high-entropy alloy) to rationalize and explain observed sintering behaviors. Furthermore, we experimentally investigated relevant interfacial phenomena (GB wetting, segregation, drying, and precipitation) to examine the underlying mechanisms.

MoNbTaW + 0–6 at.% Ni specimens were synthesized via a powder metallurgical route. High-purity powders of Nb, Ta, W (325 mesh, > 99.99% purity, < 1000 ppm O_2, Stanford Advanced Materials, CA, USA), Mo, and Ni (325 mesh, >99.95% purity, Alfa Aesar, USA) were mixed to make eight specimens of compositions listed in Suppl. Table S1. For each composition, appropriate amounts of powders were weighed out in 4 g batches. Powders were first vortex mixed for 5 min, before being high energy ball milled in a SPEX 8000D mill (SPEX SamplePrep, NJ, USA) for 1 h. Tungsten carbide lined stainless steel jars and 11.2 mm diameter tungsten carbide milling media were used with a ball-to-powder ratio of ~5:1. Milling was carried out under Ar atmosphere (< 15 ppm O_2). For each composition, ~3.6 g of the milled powder was subsequently loaded into a 10 mm diameter steel dry pressing die set (Across International, USA), and cold pressed with 400 MPa of uniaxial pressure for approximately 3 min to obtain green pellets. Green pellets were subsequently placed onto a 2 mm thick Ta substrate (>99.95% purity, Alfa Aesar), loaded into a RD-G graphite hot zone furnace (RD Webb, MA, USA), and pressure-less sintered at 1800 °C for 2 h under flowing ultra-high purity (UHP) Ar. The sintering time was selected to allow substantial densification to compare the sintering rates with and without Ni addition, while avoiding final stage grain growth and potential contamination with prolonged sintering. Ramp rates of 10 °C/min until 1500 °C and 5 °C/min thereafter were employed. Samples were then furnace-cooled under flowing UHP Ar. After sintering, samples were lightly hand ground to eliminate any surface contamination from the hot zone. Bulk density measurements were taken using measured pellet dimensions (thickness and diameter) and weighted mass. Samples were then mounted, ground, and polished for further characterization. Scanning electron microscopy (SEM) and X-ray energy dispersive spectroscopy (EDS) were conducted using a Thermo-Fisher Apreo SEM equipped with an Oxford N-Max^N EDX detector. X-ray diffraction (XRD) was performed on a Rigaku diffractometer. Transmission electron microscopy (TEM) lamellae were prepared using a Thermo-Fisher Scios DualBeam focused ion beam (FIB)/SEM. Aberration-corrected scanning transmission electron microscopy (AC STEM) high-angle annular dark field (HAADF) imaging and nanoscale EDS analyses were performed using a JEOL JEM-ARM300F microscope operating at 300 keV.
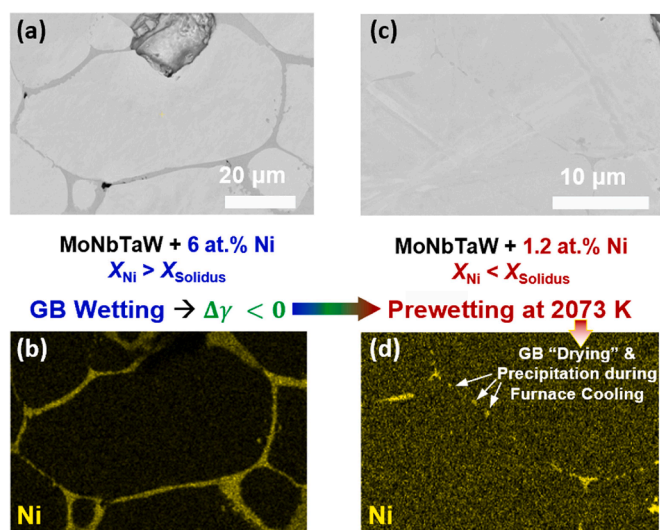
Fig. 2. (a, c) Scanning electron microscopy (SEM) images and corresponding (b, d) X-ray energy-dispersive spectroscopy (EDS) Ni maps for as-sintered (a, b) MoNbTaW-6 at.% Ni ($X_{Ni} > X_{Solidus}$) and (c, d) MoNbTaW-1.2 at.% Ni ($X_{Ni} < X_{Solidus}$) specimens. In MoNbTaW-6 at.% Ni, the Ni-enriched liquid phase wets general GBs, which proves $\Delta\gamma < 0$ (or $\gamma_{GB}^{(0)} > 2\gamma_{cl}$) and subsequently implies the possible occurrence of subsolidus GB prewetting. In MoNbTaW-1.2 at. % Ni, Ni-rich precipitates were observed along GBs (in addition to those at triple junctions), which suggests precipitation during furnace cooling (from the bulk BCC phase and/or possibly "drying" and "break-up" of prewetting films). See Suppl. Fig. S6 for additional examples (showing the generality of this observation).

To assess the BCC-liquid phase equilibria, we first assembled a thermodynamic database for Mo-Nb-Ta-W-Ni by combining the data from the 10 binary subsystems (with the interaction parameters listed in Suppl. Table S2) [29–34]. This self-assembled database only includes the BCC and liquid phases (that are sufficient as BCC and liquid are the only stable phases present at our isothermal sintering temperature of 1800 °C) and only considers binary interactions (as a simplification). CALPHAD computations were conducted using OpenCALPHAD [35]. The computed MoNbTaW-Ni isopleth using our self-assembled database and OpenCALPHAD is in good agreement with that computed from the Thermo-Calc commercial database near 1800 °C or 2073.15 K (the temperature of interest for our sintering experiments), as shown in Suppl. Fig. S1 and Table S3. The self-assembled database and CALPHAD results also served as a basis for computing the GB λ diagram in the subsequent investigation.

Next, we investigated the possible occurrence of Ni activated sintering of MoNbTaW. The measured sintered density *vs.* Ni content curve for eight MoNbTaW specimens doped with 0–6 at.% Ni and sintered at 1800 °C for 2 h is shown in Fig. 1, which shows an increase in densification with increasing Ni addition. SEM micrographs also show improved sintering characteristics of compacts with increasing Ni addition (Suppl. Fig. S3). The overall low densities (< 90% relative densities) were likely due to the large particle size of the starting powder (~45 μm in diameter) and agglomeration of ball milled particles (that produced large pores) resulting in poor sinterability. Further optimization of the starting powders (via producing high-quality and homogeneous powders using novel synthesis and processing routes, *e.g.*, gas atomization) or sintering under pressure can lead to higher relative densities. XRD spectra and EDS elemental maps of specimens doped with 0–3 at.% Ni are shown in Suppl. Figs. S4 and S5, respectively. In all cases, the primary reflections were indexed to the single-phase BCC structure, indicating the formation of high-entropy solid solutions (albeit some compositional inhomogeneity as shown in EDS maps). The Ni-enriched secondary phase was not detected by XRD, but revealed by
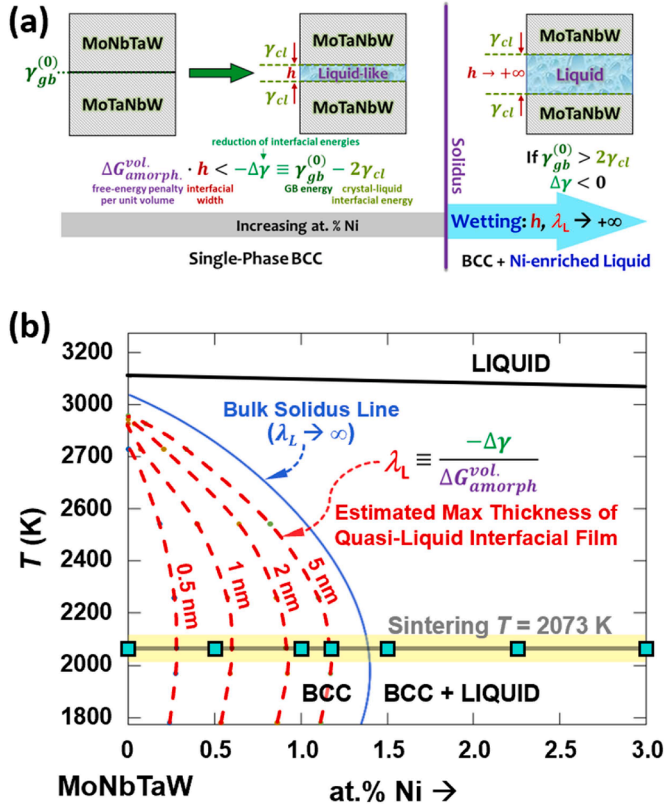
Fig. 3. (a) Schematic illustration of GB wetting (above the solidus composition) and thermodynamic stabilization of a liquid-like interfacial film at a general GB in a prewetting region below the bulk solidus composition. (b) The computed GB λ diagram plotted on the CALPHAD-computed isopleth for the MoNbTaW + x at.% Ni system. The lines of constant λ_L represent the estimated maximum thicknesses of liquid-like interfacial films that can be thermodynamically stabilized at an average general GB in Ni-doped MoNbTaW. Sintering experiments were conducted isothermally at 2073.15 K (1800 °C), where the compositions examined in this study are labeled by squares in Panel (b).

Ni EDS maps for specimens with high Ni contents (Suppl. Figs. S5 and S6).

The solidus composition at 1800 °C was determined to be ~1.39 at.% Ni using the self-assembled database and OpenCALPHAD or ~1.6 at.% Ni using the Thermo-Calc commercial database (Suppl. Table S3). For undoped MoNbTaW, the density of the sintered specimen is 8.03 g/cm³ (or only ~59% of the theoretical density, as shown in Suppl. Table S1). Adding 2.25–6 at.% Ni (above the CALPHAD-predicted bulk solidus composition) increased the sintered densities by ~32–47%. This can be attributed to liquid-phase sintering, for which the formation of a Ni-enriched liquid phase that completely wets GBs was directly confirmed by experiments, as shown by the SEM image and Ni EDS map in Fig. 2(a, b). Rounding of grains and a complete GB wetting configuration with a continuous Ni-enriched secondary phase were observable in the specimens with 2.25 at.% or higher Ni addition (as shown in Suppl. Fig. S3), indicative of liquid-phase sintering.

As a notable observation, adding 0.5–1.2 at.% Ni (below the bulk solidus composition) also increased the sintered densities by ~8–29% in the solid state. This represents the first observation of solid-state (sub-solidus) activated sintering in a high-entropy alloy. In the current case, we found that Ni can also enhance the sintering of MoNbTaW below the bulk solidus composition, akin to the well-known Ni activated sintering of Mo and W [7,8,11,19,20].

The observation of complete GB wetting, as shown in Fig. 2(a, b), implies a reduction in interfacial energies upon replacing an average "dry" GB (with the GB energy of $\gamma_{gb}^{(0)}$, where superscript "(0)" denote a

hypothetical GB without interfacial disordering and Ni segregation) with two crystal-liquid interfaces (with the total interfacial energies of $2\gamma_{cl}$):

$$\Delta\gamma \equiv 2\gamma_{cl} - \gamma_{gb}^{(0)} < 0 \tag{1}$$

Using the statistical thermodynamic models and equations described in Ref. [24], we estimated that $\gamma_{cl} \approx 0.3475$ J/m² and $\gamma_{GB}^{(0)} \approx 1.19$ J/m² at the sintering temperature of 1800 °C (2073.15 K), which produced $\Delta\gamma$ of -0.495 J/m² (< 0), consistent with the observed complete GB wetting. The elemental property data used for the calculations are given in Suppl. Table S4.

The occurrence of complete GB wetting ($\Delta\gamma < 0$, which is also supported by evaluation using the statistical models discussed above) above the bulk solidus composition logically infers the existence of a prewetting region below the bulk solidus composition. Here, "prewetting" refers to GB wetting by a liquid-like film occurring when the liquid is not yet a stable bulk phase (at $X_{Ni} < X_{solidus}$) [21]. As shown in Fig. 3(a), a liquid-like interfacial film of thickness h can be thermodynamically stabilized at a general GB in a prewetting region ($X_{Ni} < X_{solidus}$) if the volumetric free-energy penalty ($\Delta G_{amorph.}^{vol.}$) to form the undercooled liquid can be over-compensated by the reduction in interfacial energies ($-\Delta\gamma$), or:

$$\Delta G_{amorph.}^{vol.} \cdot h < -\Delta\gamma. \tag{2}$$

Following prior studies of binary and ternary alloys [20,22-27], we can define a thermodynamic parameter, λ, to represent the thermodynamic tendency for an averaged general GB to disorder (*i.e.*, stabilizing a liquid-like interfacial film) in the prewetting region:

$$\lambda = \frac{-\Delta\gamma}{\Delta G_{amorph.}^{vol.}}, \tag{3}$$

Here, we quantified $\Delta G_{amorph.}^{vol.}$ from bulk CALPHAD data (using our self-assembled database):

$$\Delta G_{amorph.}^{vol.}\left(X_{BCC}, X_{film}^L\right) = \frac{G^L\left(X_{film}^L\right) - \sum_i \mu_i^{BCC} X_i^L}{\sum_i V_i X_i^L} \tag{4}$$

where $G^L(X_{film}^L)$ is the molar free energy of the liquid phase, $X_{film}^L = \{X_i^L\}$ is the vector composition of the interfacial film, X_{BCC} is the vector composition of the BCC phase, μ_i^{BCC} is the chemical potential of the BCC phase, and $\sum_i V_i X_i^L$ is the molar volume of the liquid phase. We can then rewrite Eq. (3) for the MoNbTaW-Ni system as:

$$\lambda_L\left(X_{Ni}^{BCC}, T\right) = \frac{\gamma_{gb}^{(0)}(X_{BCC}) - 2\gamma_{cl}\left[X_{BCC}, X_{liquidus}(T)\right]}{\Delta G_{amorph.}^{vol.}\left[X_{BCC}, X_{liquidus}(T)\right]}, \tag{5}$$

where λ_L is calculated assuming that the interfacial film is a uniform, perfect liquid adopting the temperature-dependent bulk liquidus composition, *i.e.*, $X_{film}^L = X_{liquidus}(T)$, which is of one the conventions proposed and tested previously [25]. Here, the vector X_{BCC} is a function of scalar Ni atomic fraction X_{Ni}^{BCC} only (as Mo, Nb, Ta, and W are kept equiatomic). Again, we estimated $\gamma_{GB}^{(0)} = \gamma_{gb}^{(0)}(X_{BCC})$ and $\gamma_{cl} = \gamma_{cl}[X_{BCC}, X_{liquidus}(T)]$ using the statistical thermodynamic models and equations described in Ref. [24]. Subsequently, we computed $\lambda_L(X_{Ni}^{BCC}, T)$ as a function of the Ni atomic fraction in the BCC phase ($X_{Ni} = X_{Ni}^{BCC}$) and temperature (T) to construct a GB λ diagram in Fig. 3(b), where red dashed lines of constant λ_L values were plotted in the bulk MoNbTaW-Ni isopleth. See Suppl. Note S1 for the detailed procedure to compute a GB λ diagram. Suppl. Table S5 documents the calculated values of X_{Ni}^{BCC} for constant values of λ_L that were used to construct the GB λ diagram shown in Fig. 3(b). Here, the computed λ_L value represents the estimated maximum thickness of the liquid-like interfacial film that can be thermodynamically stabilized at an average general GB, and it scales the
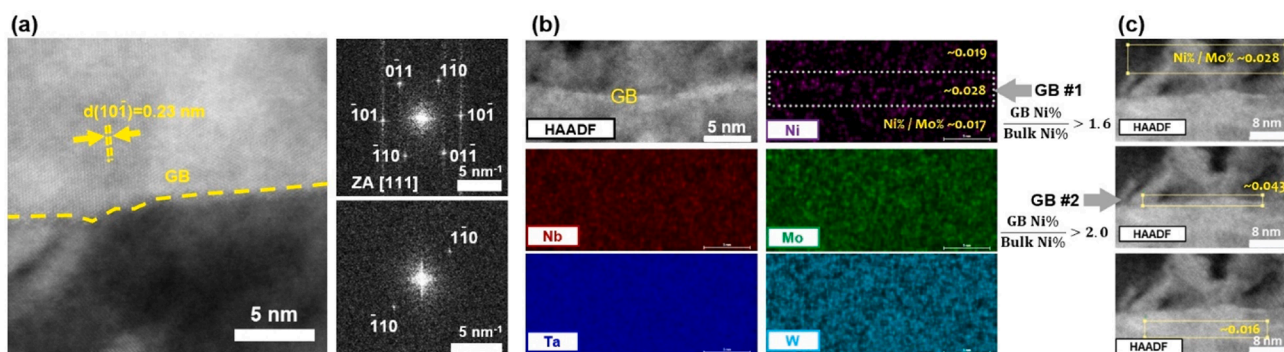
Fig. 4. (a) Aberration-corrected scanning transmission electron microscopy (AC STEM) image of a GB region in MoNbTaW-1.2 at.% Ni, along with selective area electron diffraction (SAED) patterns viewed along the [111] zone axis. (b) STEM and EDS elemental maps of a GB region. Weak GB segregation of Ni was evident via a quantitative analysis shown in Suppl. Fig. S9. (c) Weak GB segregation of Ni was also observed for another (independent) GB via a quantitative analysis of STEM box scans on the GB and inside the two abutting grains; see Suppl. Fig. S10 for the detailed analysis. For both GB #1 and GB #2, the actual GB-to-bulk Ni wt.% ratios should be larger than 1.6 and 2.0 (labeled in the figure), respectively, because the width of STEM scanning box at the GB is likely larger than the thickness of the GB segregation zone and the GBs are curved (so that GB measurements represent the averaged compositions over larger regions). The absolute quantification of elements is inaccurate because of the EDS peak overlaps, but weak segregation of Ni can be concluded from the analyses shown in Suppl. Figs. S9 and S10 confidently.

actual equilibrium interfacial width ($h_{eq.}$) [20,22-27]. Note that $\lambda_L \to \infty$ at the bulk solidus composition, where the thickness of the prewetting film is divergent as complete GB wetting takes place.

The computed GB λ diagram shown in Fig. 3(b) suggests the possible thermodynamic stabilization of a liquid-like interfacial film in a wide prewetting region. As prior studies of binary and ternary refractory alloys suggested, the onset activated sintering typically corresponds to computed λ values of ~0.5–1 nm [20,22-27], where subsolidus activated sintering was indeed observed for the current study of Ni activated sintering of MoNbTaW (for X_{Ni} = 0.5–1.2 at.%). Thus, it is possible that Ni activated sintering of MoNbTaW resulted from enhanced mass transport in the liquid-like GBs formed in the prewetting region, akin to the simpler systems of Ni activated sintering of Mo and W reported previously [19,20]. Nonetheless, we recognize that other factors, such as formation of a transient liquid or improved bulk diffusion, can also exist and contribute to the enhanced sintering.

Fig. 4 shows results from the AC STEM and EDS analyses of two general GBs in sintered MoNbTaW-1.2 at.% Ni, where we only observed weak GB segregation of Ni in the furnace-cooled specimen. Quantitative STEM-EDS analyses on the GB regions and the neighboring grains (as shown in Suppl. Figs. S9 and S10) suggest the GB-to-bulk Ni wt.% ratios are greater than 1.6 and 2.0, respectively, for measurements at two independent GBs. The actual GB-to-bulk Ni wt.% ratios are likely even higher because the widths of STEM scanning boxes at the GBs are larger than the thickness of the GB segregation zones, and the GBs are curved. Nonetheless, the observed segregation of Ni is weak, suggesting possible GB drying (possibly break-up of the nanoscale prewetting films) during slow cooling in the furnace-cooled specimens (~25 °C/min from 1800 °C to 1000 °C). Furthermore, nanoscale precipitates were observed along general GBs (in addition to those at triple junctions) in furnace-cooled MoNbTaW-1.2 at.% Ni, as shown in Fig. 3(d) and Suppl Fig. S6, which is consistent with "drying" or break-up of nanoscale prewetting films during cooling, with additional precipitation from the bulk BCC phase (as the Ni solubility decreases with decreasing temperature). Similar weak GB segregation results were also observed in MoNbTaW-1.0 at.% Ni (Suppl. Figs. S11 and S12), where the GB-to-bulk Ni wt.% ratios were suggested to be greater than 1.26 and 1.18, respectively, from measurements of two independent GBs. Ni segregation was also observed at the interface of a MoNbTaW grain and a secondary carbide precipitation (Suppl. Figs. S13 and S14). Future studies of quenched specimens or *in-situ* experiments (both of which are beyond our current equipment capabilities) may clarify the cooling effects. GB drying during cooling in Ni-doped MoNbTaW, if it indeed occurred, may alleviate GB embrittlement to circumvent a common side-effect of

activated sintering of refractory metals [11].

Based on prior experimental and modeling studies of Ni-activated sintering of W and Mo in simpler binary systems [7,8,17,19,26,27], the onset of solid-state activated sintering can take place at lower temperatures (*e.g.*, 1000–1300 °C). It is possible that Ni-activated sintering of NbMoTaW can occur at comparable temperatures (below the lowest solidus temperature of the quinary system), particularly if high-quality, homogenous, non-agglomerated powders were available and used. Based on the proposed mechanism, the "activator" (sintering aid) should segregate at GBs to promote interfacial disordering to subsequently enhance sintering. The selection of sintering aids (Ni or other transition metals) and sintering conditions can be guided by the interfacial thermodynamic model and computed GB λ diagrams.

In summary, this study revealed the first example of activated sintering of high-entropy alloys – Ni activated sintering of MoNbTaW. Complete GB wetting was confirmed experimentally above the bulk solidus composition, which logically inferred the stabilization of nanoscale liquid-like interfacial films in a prewetting region below the bulk solidus composition. Subsequently, a GB λ diagram was computed for MoNbTaW-Ni to forecast high-temperature GB disordering in the prewetting region, and subsequently rationalize observed Ni activated sintering of MoNbTaW. Only weak GB segregation of Ni and precipitation along GBs were found in furnace-cooled subsolidus sintered specimens, suggesting that GB drying might have occurred during slow cooling.

Declaration of Competing Interest

The authors declare that they have no known competing financial interests or personal relationships that could have appeared to influence the work reported in this paper.

Acknowledgement

calculation results shown in the Supplementary Materials for benchmarking our self-assembled database and calculations using OpenCALPHAD.

Supplementary materials

Supplementary material associated with this article can be found, in the online version, at doi:10.1016/j.scriptamat.2023.115777.

References

[1] O. Senkov, G. Wilks, D. Miracle, C. Chuang, P. Liaw, Intermetallics 18 (9) (2010) 1758–1765.
[2] O.N. Senkov, D.B. Miracle, K.J. Chaput, J.-P. Couzinie, J. Mater. Res. 33 (19) (2018) 3092–3128.
[3] T. Li, W. Jiao, J. Miao, Y. Lu, E. Guo, T. Wang, T. Li, P.K. Liaw, Mater. Sci. Eng.: A 827 (2021), 142061.
[4] T. Li, J. Miao, Y. Lu, T. Wang, T. Li, Int. J. Refract. Metals Hard Mater. 103 (2022), 105762.
[5] T. Li, S. Wang, W. Fan, Y. Lu, T. Wang, T. Li, P.K. Liaw, Acta Mater. 246 (2023), 118728.
[6] R.M. German, P. Suri, S.J. Park, J. Mater. Sci. 44 (2009) 1–39.
[7] H.W. Hayden, J.H. Brophy, J. Electrochem. Soc. 110 (1963) 805–810.
[8] R.M. German, Rev. Powder Metallurg. Phys. Ceramic. 2 (1982) 9–43.
[9] R. German, Z. Munir, Powder Metallurg. 20 (3) (1977) 145–150.
[10] R.M. German, B. Rabin, Powder Metallurg. 28 (1) (1985) 7–12.
[11] K. Hwang, H. Huang, Acta Mater. 51 (13) (2003) 3915–3926.
[12] J. Luo, H. Wang, Y.-M. Chiang, J. Am. Ceramic Soc. 82 (1999) 916.
[13] J. Nie, J.M. Chan, M. Qin, N. Zhou, J. Luo, Acta Mater. 130 (2017) 329–338.
[14] P.R. Cantwell, M. Tang, S.J. Dillon, J. Luo, G.S. Rohrer, M.P. Harmer, Acta Mater. 62 (2014) 1–48.
[15] M. Tang, W.C. Carter, R.M. Cannon, Phys. Rev. B 73 (2) (2006), 024102.
[16] M. Tang, W.C. Carter, R.M. Cannon, Phys. Rev. Lett. 97 (7) (2006), 075502.
[17] J. Luo, V.K. Gupta, D.H. Yoon, H.M. Meyer, Appl. Phys. Lett. 87 (2005), 231902.
[18] X. Shi, J. Luo, Appl. Phys. Lett. 94 (25) (2009), 251908.
[19] V.K. Gupta, D.H. Yoon, H.M. Meyer III, J. Luo, Acta Mater. 55 (2007) 3131–3142.
[20] X. Shi, J. Luo, Phys. Rev. B 84 (1) (2011), 014105.
[21] J. Luo, Crit. Rev. Solid State Mater. Sci. 32 (1–2) (2007) 67–109.
[22] J. Luo, Interdiscip. Mater. 2 (1) (2023) 137–160.
[23] N. Zhou, T. Hu, J. Luo, Curr. Opin. Solid State Mater. Sci. 20 (2016) 268–277.
[24] N.X. Zhou, J. Luo, Acta Mater. 91 (2015) 202–216.
[25] J. Luo, J. Am. Ceramic Soc. 95 (8) (2012) 2358–2371.
[26] J. Luo, X. Shi, Appl. Phys. Lett. 92 (10) (2008) 101901.
[27] J. Luo, Curr. Opin. Solid State Mater. Sci. 12 (5/6) (2008) 81–88.
[28] M. Qin, S. Shivakumar, J. Luo, J. Mater. Sci. 58 (20) (2023) 8548–8562.
[29] P. Turchi, V. Drchal, J. Kudrnovský, C. Colinet, L. Kaufman, Z.-K. Liu, Phys. Rev. B 71 (9) (2005), 094206.
[30] J. Shi, C. Guo, C. Li, Z. Du, Calphad 76 (2022), 102381.
[31] Y. Li, C. Li, Z. Du, C. Guo, Calphad 43 (2013) 112–123.
[32] M. Tang, Y. Du, P. Zhou, S. Wang, H. Zhang, Y. Zeng, S. Liu, X. Chai, Y. Peng, C. Wu, Calphad 68 (2020), 101748.
[33] W. Xiong, Y. Du, Y. Liu, B. Huang, H. Xu, H. Chen, Z. Pan, Calphad 28 (2) (2004) 133–140.
[34] I. Ansara, M. Selleby, Calphad 18 (1) (1994) 99–107.
[35] B. Sundman, U.R. Kattner, M. Palumbo, S.G. Fries, Integrat. Mater. Manuf. Innovat. 4 (2015) 1–15.